International Journal of Heat and Mass Transfer 53 (2010) 5400–5410

Contents lists available at ScienceDirect

International Journal of Heat and Mass Transfer

journal homepage: www.elsevier.com/locate/ijhmt

Direct numerical simulation of turbulent flow and combined convective heat transfer in a square duct with axial rotation

Xiang Yang, Zeng-Yao Li, Wen-Quan Tao *

School of Energy and Power Engineering, Xi'an Jiaotong University, Xi'an 710049, China

ARTICLE INFO

Article history:
Available online 5 August 2010

Keywords:
Direct numerical simulation
Turbulent flow
Mixed convection
Rotation
Buoyancy force

ABSTRACT

Direct numerical simulations (DNS) of turbulent flow and convective heat transfer in a square duct with axial rotation were carried out. The pressure-driven flow is assumed to be hydrodynamically and thermally fully developed, for which the Reynolds number based on the friction velocity and hydraulic diameter is kept at constant ($Re_\tau = 400$). In the finite length duct, two opposite walls are perfectly insulated and another two opposite walls are kept at constant but different temperatures. Four thermal boundary conditions were chosen in combination with axial rotation to study the effects of rotation and Grashof number on mean flow, turbulent quantities and momentum budget. The results show that thermal boundary conditions have significant effects on the topology of secondary flows, profiles of streamwise velocity, distribution of temperature and other turbulent statistic quantities but have marginal effects on the bulk-averaged quantities; Coriolis force affects the statistical results very slightly because it exerts on the plane normal to main flow direction and the rotation rate is low; Buoyancy effects on the turbulent flow and heat transfer increase with the increase of Grashof number (Gr), and become the major mechanism of the development of secondary flow, turbulence increase, and momentum and energy transport at high Grashof number.

1. Introduction

Turbulent flow and heat transfer in an axially rotating duct often occur in practical engineering applications, such as in compact heat exchangers, cooling channel in gas turbines and other rotary machineries. Because of rotation, Coriolis force and centrifugal force give rise to so-called persistent secondary flows, hence, the streamwise velocity becomes asymmetric about its center. Eventually, the substantial change of flow field brings about variations of temperature field and heat transfer.

Many researchers have concentrated to investigate the rotation effect on turbulent flow and heat transfer. Experimental and numerical studies in turbulent channel flow subjected to rotation being parallel or perpendicular to walls were carried out in Refs. [1–4]. In these literatures, it is well established that interaction between Coriolis force and the mean shear induces stabilization and destabilization in suction side and pressure side, respectively, and rotation causes development and drift of large-scale counter-rotating roll cells. For the duct flow, extensive experimental investigations [5,6] and numerical studies have been performed in stationary duct [7–9]. Pallares and Davidson [10,11] did large eddy simulations (LES) of turbulent flow and mixed heat transfer in both stationary and orthogonally rotating square ducts. They identified that rotation can induces obvious changes in flow field and temperature distribution. Qin and Pletcher [12] studied turbulent mixed convective heat transfer in a thermally developing orthogonally rotating square duct flow by using LES. But to the author's knowledge few DNS and LES results are available for axially rotating duct flow.

This paper presents the influences of thermal boundary conditions, rotation rate and Grashof number on the mean flow, temperature distribution and turbulent statistical quantities as well as momentum budget in an axially rotating square duct flow. In order to take into account the effects of thermal boundary conditions, four different thermal boundary conditions are studied at different rotation rate and different Grashof number. In the following presentation, the mathematical model and numerical methods of DNS are first briefly provided, followed by a validation of the developed code. Then the simulation results are presented, including the mean flow and temperature fields, the turbulence intensities, the momentum budget, and turbulent structures. Finally some conclusions will be made.

2. Model and numerical methods

Fig. 1 shows the physical model of the straight duct and coordinate system adopted. The entire system rotates with positive angular

* Corresponding author.
E-mail address: wqtao@mail.xjtu.edu.cn (W.-Q. Tao).

0017-9310/$ - see front matter © 2010 Published by Elsevier Ltd.
doi:10.1016/j.ijheatmasstransfer.2010.07.016

Nomenclature

F_i	source term of momentum equations in *i*-direction
Gr	Grashof number, $(R\omega^2)\beta(T_h - T_c)H^3\nu^2$
g	gravitational acceleration (m/s^2)
H	width of duct (m)
k	turbulent fluctuating kinetic energy (m^2/s^2)
L	length of duct (m)
Nu	Nusselt number, $Nu = q_w H(\lambda \Delta T)$
Pr	molecular Prandtl number
Re_τ	turbulent Reynolds number, $Re_\tau = u_\tau H/\nu$
Ro	rotation number, $Ro = 2H\Omega u_\tau$
T_c	the temperature on the cold wall (K)
T_h	the temperature on the hot wall (K)
u, v, w	dimensionless velocity components in *x*-, *y*- and *z*-directions
U_b	bulk averaged streamwise velocity
u_τ	friction velocity, $\sqrt{\tau_w/\rho}$
p	dimensionless pressure
x, y, z	Cartesian coordinates (m)
y_0, z_0	coordinates of rotation axis in *y*–*z* plane
x^+, y^+, z^+	wall coordinates

Greek

β	thermal expansion coefficient (1/K)
δ_{ij}	Kronecker delta
ΔT	temperature difference, $T_h - T_c$ (K)
Θ	dimensionless temperature
λ	thermal conductivity (W/(m K))
ν	kinematic viscosity (m^2/s)
Ω	rotational angle velocity (rad s^{-1})
Ω_j	components of Ω
ω	norm of Ω
ρ	density (kg/m^3)
τ_w	wall shear stress (N/m^2)
$\langle\rangle$	ensemble average in the *x*-direction and in time

Subscripts

m	mean
b	bulk average
rms	root-mean-square fluctuation
w	wall
′	fluctuating value

velocity, Ω, with the rotation axis being through the center of duct and parallel to the *x*-direction. The coordinates in the vertical, normal and spanwise directions are x, y and z, respectively, and the instantaneous velocities u, v and w are specified in the corresponding directions. The flow is driven by externally imposed mean pressure gradient between the inlet and outlet, and assumed to be hydrodynamically and thermally developed. The four walls are smooth, and during the process of rotation constant but different temperatures are imposed on the two opposite walls which are perpendicular to another two opposite walls insulated perfectly. So four thermal boundary conditions are obtained: Case 1, the left and right walls keep adiabatic, the bottom wall keeps hot and the top wall keeps cold; Case 2, the bottom and top walls keep adiabatic, the left wall keeps hot and the right wall keeps cold; Case 3, the left and right walls keep adiabatic, the bottom wall keeps cold and the top wall keeps hot; Case 4, the bottom and top walls keep adiabatic, the left wall keeps cold and the right wall keeps hot. The physical properties of the fluid are assumed to be constant with temperature with Pr = 0.71. Only a linear dependence of the temperature on density is taken into account to model the buoyancy effect according to the Boussinesq approximation [13].

The governing equations are the three-dimensional, time-dependent Navier–Stokes equations, continuity equation and energy equation. They can be expressed in dimensionless form in rotational coordinate system as follow [10,11]:

$$\frac{\partial u_i}{\partial x_i} = 0 \tag{1}$$

$$\frac{\partial u_i}{\partial t} + \frac{\partial(\rho u_i u_j)}{\partial x_j} = -\frac{\partial p}{\partial x_i} + \frac{1}{Re_\tau}\frac{\partial}{\partial x_j}\left(\frac{\partial u_i}{\partial x_j}\right) + F_i \tag{2}$$

$$\frac{\partial \Theta}{\partial t} + \frac{\partial(u_j\Theta)}{\partial x_j} = \frac{1}{\mathrm{Re}_\tau \mathrm{Pr}}\frac{\partial}{\partial x_j}\left(\frac{\partial \Theta}{\partial x_j}\right) \tag{3}$$

$$F_i = \begin{pmatrix} 4\delta_{i1} \\ Row - (y - y_0)\frac{Gr}{\mathrm{Re}_\tau^2}\Theta \\ -Ro\,v - (z - z_0)\frac{Gr}{\mathrm{Re}_\tau^2}\Theta \end{pmatrix} \tag{4}$$

The hydraulic diameter (H), averaged friction velocity (u_τ), and temperature difference ($\Delta T = T_h - T_c$) are used as the characteristic scales for the length, velocity, temperature, respectively. Formulation (4) is the expression of source term in Eq. (3), corresponding to three velocity components u, v, w, respectively. In Formulation (4), $4\delta_{i1}$ is the mean pressure gradient, Row and $-Rov$ are the Coriolis force terms, $(y - y_0)Gr/Re_\tau^2\Theta$ and $(z - z_0)Gr/Re_\tau^2\Theta$ are the centrifugal buoyancy terms with respect to v and w momentum equations, respectively.

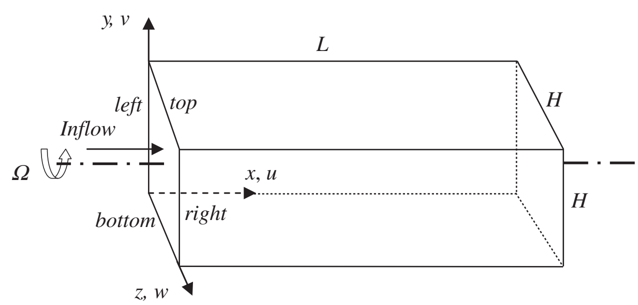

Fig. 1. Physical model and coordinate system.

The non-slip boundary conditions in the walls were adopted for the velocities. For the temperature, four thermal boundary conditions mentioned above were adopted, respectively. In *x*-direction periodic boundary conditions were employed.

A uniform grid was employed in the *x*-direction and nonuniform grids were used in the *y*- and *z*-directions. The momentum and energy equations were discretized by the second-order accurate central difference scheme on staggered grids and advanced with a fractional-step method. The second-order Adams–Bashforth time discretization was used. A Poisson pressure correction equation was used to enforce continuity, and it was solved by Gauss–Seidel iteration method. The convergence criterion of the Poisson equation requires that the maximum residual of the equation is less than a prespecified small value of 10^{-7} .To speed-up the calculation procedure, parallel computing technique based on MPI was adopted. The computational parameters are summarized in Table 1.

Table 1
Computational parameters.

Domain	Grids	Grid spacing		Time increment	Grid spacing in wall coordinates	
		x	y, z		x^+	y^+, z^+
$6.4H \times H \times H$	$256 \times 128 \times 128$	$0.025H$	$0.0015H$–$0.0127H$	$5 \times 10^{-5} H/u_\tau$	10	0.6–5.08

The sampling procedure used to obtain the turbulent statistical quantities was not started until the flow was fully developed. The representative results averaged in the x-direction and time were carried out for about 50 nondimensional time units according to Ref. [10].

3. Validation

Simulations were conducted for shear Reynolds number $Re_\tau = 400$. For validating code developed by ourselves we have to find some benchmark cases. To the author's knowledge there is no benchmark solution to the axially rotating duct flow taking into account buoyancy. Some previous DNS results are only for the turbulent flow in a stationary duct at low Reynolds number and they are used to validate our self-developed code before the simulated turbulent statistical quantities are shown. Fig. 2 displays the DNS turbulent statistic results simulated by our codes in a stationary duct flow for which the two horizontal walls are assumed to be at constant but different temperatures with the bottom being hot, and the vertical walls are assumed to be insulated. Fig. 2(a) shows that the streamwise velocity in wall coordinates fits well with the law of the wall in the viscous layer; but a little difference exists in the logarithm regime which also occurs in Ref. [8]. The Reynolds stresses are compared with the previous LES results of Kajishima and Miyake with the same turbulent Reynolds number $Re_\tau = 400$ [14], which shows the solutions are in good agreement along the bisectors over the whole duct. But there is no temperature information in [14], so we have to compare the temperature with the available DNS results of Piller and Nobile [9] for $Re_\tau = 300$ (Fig. 2(b)). Some deviation exists in the lower y region, but the agreement can be regarded as acceptable.

The grid system adopted in our computation was $256 \times 128 \times 128$. It should be noted that we did not conduct the grid-refinement study due to the limitation of computational resources. However, as indicated in Fig. 2 we compared our solution with that of Refs. [8,9]. Huser and Biringen [8] conducted DNS of turbulent flow

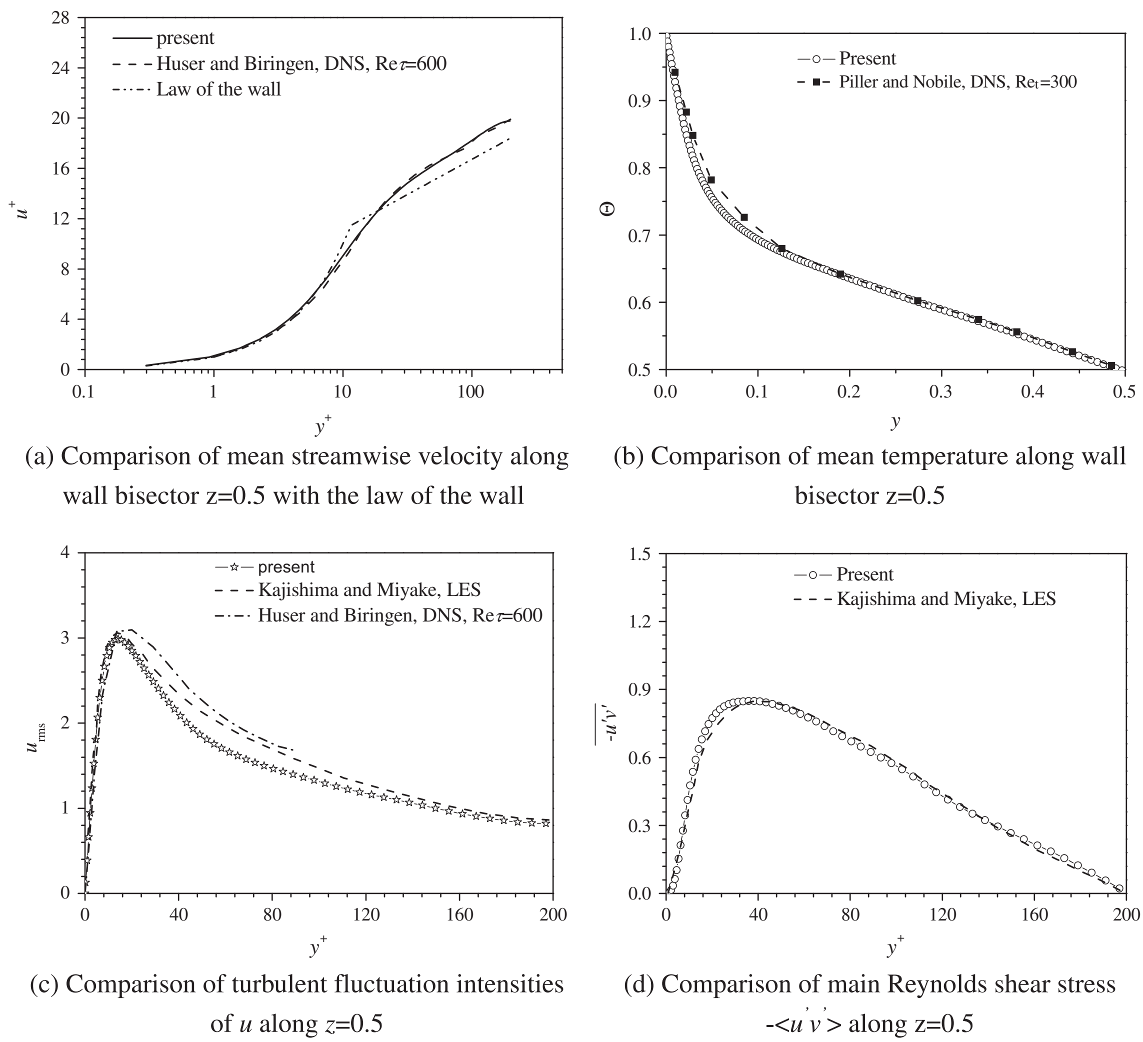

(a) Comparison of mean streamwise velocity along wall bisector z=0.5 with the law of the wall

(b) Comparison of mean temperature along wall bisector z=0.5

(c) Comparison of turbulent fluctuation intensities of u along z=0.5

(d) Comparison of main Reynolds shear stress $-\langle u'v' \rangle$ along z=0.5

Fig. 2. Results comparison of validation case with previous DNS solutions.

($Re_\tau = 600$) in a square duct using two sets grids ($64 \times 81 \times 81$ and $96 \times 101 \times 101$) in a computational domain $6.4D \times D \times D$ (D is the height of the duct). The convective terms were discretized by fifth-order upwind-biased finite difference scheme and the viscous terms were discretized by fourth-order central difference scheme. Piller and Nobile [9]conducted DNS of turbulent heat transfer in a square duct using only one set grid ($200 \times 127 \times 127$) in a computational domain $6.28D \times D \times D$ (D is the height of the duct), and the second-order central difference scheme was used to the spacial discretization. The reasonably good agreement shown in Fig. 2 indicates that the resolution in our paper can be considered as acceptable, at least for a start phase investigation.

4. Results and discussion

The hydrodynamically and thermally fully developed pressure-driven flow shown in Fig. 1 is simulated by DNS for the Reynolds number based on the friction velocity of 400 ($Re_\tau = 400$). In the following the mean flow properties will first be presented, followed by the predicted turbulence intensities and momentum budget. Finally the turbulent structure will be provided.

4.1. Mean flow properties

Fig. 3 shows the isotachs of the mean streamwise velocity (solid lines), isothermals (dashed lines), and secondary flow vectors in cross-section plane for different wall thermal boundary conditions.

In Fig. 3(a), the distributed pattern of the streamwise velocity is quite similar to that of nonrotating case [15] at first glance. However after careful comparison, there are following three differences. First the present isotachs of the streamwise velocity in the left-upper and right-lower corner regions clearly bend toward the corners. Second, in the present simulation the values of mean streamwise velocity decrease compared to those in [15]. Third, the isotachs in [15] are symmetrical about the wall bisector $z = 0.5$ (i.e., left–right symmetry), while in the present case some similarity exists between the isotachs in the left-upper corner and right-lower corner regions (i.e., diagonally left–right symmetry) and the same feature exists for the distribution of right-upper and left-lower corner regions. Such variation of the streamwise velocity distribution may be attributed to the Coriolis force and centrifugal buoyancy force. The secondary flows in Fig. 3(a) are mainly constructed by a large cell and four small cells in corners. The circulation brings the fluid in the hot side in the region of $z < 0.5$ to the cold side, and brings the cold fluid in the region of $z > 0.5$ to the hot side. The temperature contours in the left-upper corner and right-lower corner are somewhat bent because of the small secondary cells in these corners.

Compared with Fig. 3(a), the results shown in Fig. 3(b) have following features. First the contours of the mean streamwise velocity bend towards the upper-right and lower-left corners, and the

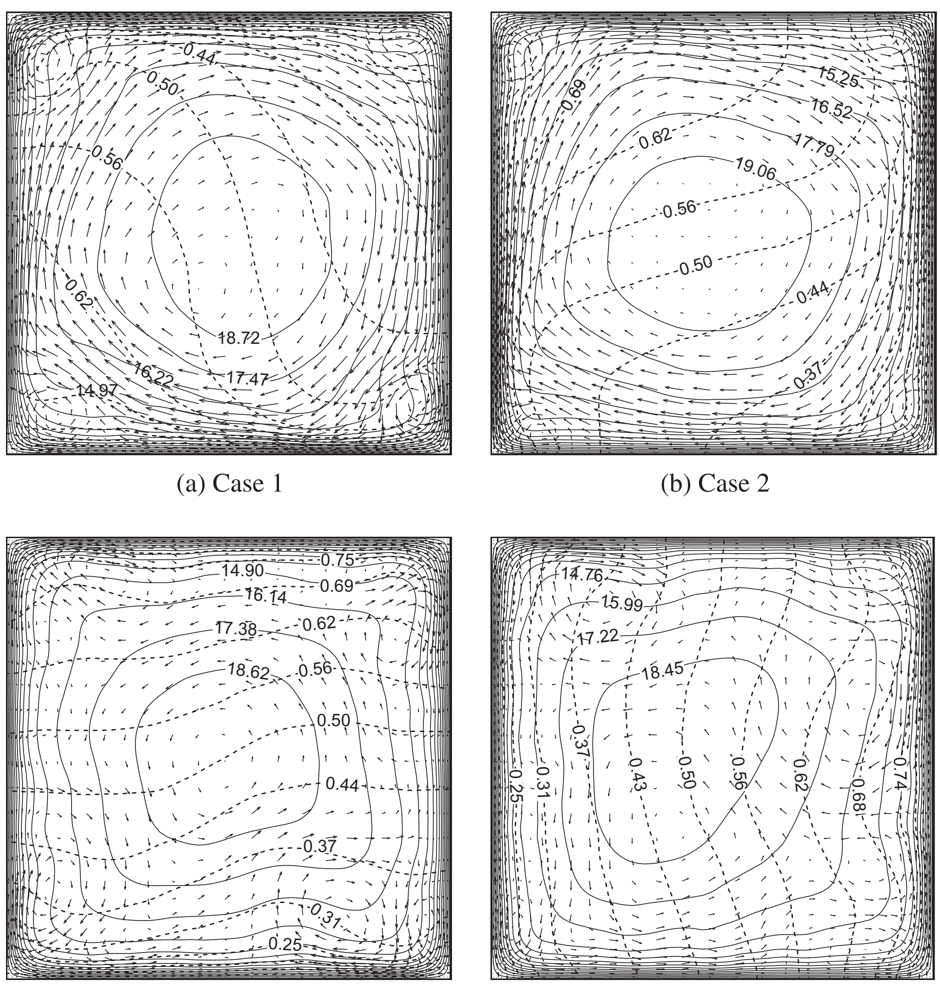

(a) Case 1 (b) Case 2

(c) Case 3 (d) Case 4

Fig. 3. Velocity and temperature field for different cases ($Gr = 10^6$, $Ro = 5.0$) corresponding to different thermal boundary conditions.

streamwise velocity increases. Second, although the configuration of secondary cells is qualitatively the same as Fig. 3(a) with one large cell being dominant in the center, but the circulation intensity decreases and small ones in the corners are stretched. Third, the temperature increases from the lower-right region to the upper-left region rather than from lower-left region to the upper-right region in Fig. 3(a).

In Fig. 3(c) a quite different flow field and isothermals distribution can be observed. For this case the upper and lower walls are at high and low temperatures and the two vertical walls are adiabatic. Hence the isotachs of the streamwise velocity are very similar to the case of a stationary duct flow without centrifugal buoyancy. In addition the isothermals are more or less parallel to the top/bottom walls. This is because the temperature gradient is positive and the density gradient is negative along positive y-direction, which means that nearly no buoyancy is induced. The similarity of the flow and temperature fields between the present case and that of a stationary duct flow indicates that Coriolis force has small effects on the secondary flows at the present Grashof number and rotation rate. The intensities of secondary flow are remarkably reduced and the four small secondary cells are drifted a bit towards the wall bisectors.

Attention is now turned to the last case. In Fig. 3(d), the contours of the streamwise velocity become more irregular with its gradient in the left side being higher than that of the right side. The isothermals are almost parallel to the vertical walls, which is consistent with the thermal boundary condition. The secondary flow patterns are drastically changed and there is no dominant circulation in the cross section only with two small cells near the upper and right walls.

Fig. 3 shows that contour lines and secondary flow topology are quite different with different thermal boundaries. However, Table 2 shows that the bulk averaged velocity U_b, turbulence level and friction factor have no obvious differences for the four cases. But Nusselt numbers of Case 3 and Case 4 change drastically compared with those of Case 1 and Case 2. There is a reduction of overall averaged Nusselt number of Case 3 because of no buoyancy. While the increase of Nusselt number of Case 4 may be attributed to the increase of the overall turbulence level.

Fig. 4 demonstrates the influences of Grashof number and rotation rate on the temperature contours (long-dashed line for $Ro = 0.1$, short-dash line for $Ro = 5.0$), streamwise velocity isotaches (solid line) and secondary flow vectors for Case 1. With the increase of Grashof number from $Gr = 10^6$ to $Gr = 10^8$, the distributions of the cross-section flow fields, temperature and streamwise velocity fields are dramatically changed. Compared with the nonrotating case [15], the intensities of the secondary flow are reduced in Fig. 4(a), which means that rotation weakens the secondary flow. Also the profiles of axial velocity and temperature are a little different from those of stationary duct flow. Fig. 4(b) ($Ro = 5.0$, $Gr = 10^6$) shows that the increase of Ro from 0.1 to 5.0 makes the topology of cross-section flow field a little different from that of Fig. 4(a) with slight reduction of secondary-flow intensities in the whole region. But the steamwise velocity and temperature fields have no obvious change compared to Fig. 4(a). These indicate that Coriolis force has a little influence on the flow and temperature fields in an axially rotating duct flow. In Fig. 4(c) the Grashof number increases to 10^7, and it shows that the cross-section velocity field consists of one large cell in the center and two small cells near the two bottom corners. The large cell generated by the buoyancy convects hot low momentum fluid from the bottom wall to the top wall and then this stream returns (Fig. 4(c)). What's more interesting is the existence of a narrow long region extending to the top left of the duct, where there is a very weak ascending flow. The small cell near the down left corner is enlarged but another small cell near down right corner becomes smaller compared with Fig. 4(b). The convective transport induced by the ascending currents in the central part of the duct displaces the maximum value of the streamwise velocity component and the minimum value of the temperature towards the top right side of the duct. The temperature contours bulge toward the top wall and deviate from the right half of the duct. At Grashof number $Gr = 10^8$, the secondary flow becomes stronger compared to that of $Gr = 10^7$ because of the increased buoyancy force (Fig. 4(d)). Here as the case shown above one large cell dominates the cross section flow with a small cell being near the down left corner. A narrower region containing weak secondary flow near the left wall still exists, but the small cell near down right corner disappears. Enhanced ascending flow drives low momentum and hot fluid from the bottom wall, across central part of the duct, to the top right side. Near the right wall and top right side streamwise velocity component increases but decreases near the bottom wall and down left side compared with Fig. 4(c). The temperature contours also show the same tendency as the streamwise velocity.

As indicated above, the patterns and intensities of the secondary flow are changed for different cases and different Grashof numbers. This is mainly resulted from the forces balance in cross section. The analysis is conducted as follows. The Reynolds-averaged equations for the cross-section flow are written as,

$$\langle v\rangle\frac{\partial\langle v\rangle}{\partial y}+\langle w\rangle\frac{\partial\langle v\rangle}{\partial z}=-\frac{\partial\langle p\rangle}{\partial y}+\frac{1}{Re_\tau}\left(\frac{\partial^2\langle v\rangle}{\partial y^2}+\frac{\partial^2\langle v\rangle}{\partial z^2}\right)-\frac{\partial\langle v'v'\rangle}{\partial y}-\frac{\partial\langle v'w'\rangle}{\partial z}+Ro\tau_1\langle w\rangle-(y-y_0)\frac{Gr}{Re_\tau^2}\langle\Theta\rangle \tag{5}$$

$$\langle v\rangle\frac{\partial\langle w\rangle}{\partial y}+\langle w\rangle\frac{\partial\langle w\rangle}{\partial z}=-\frac{\partial\langle p\rangle}{\partial z}+\frac{1}{Re_\tau}\left(\frac{\partial^2\langle w\rangle}{\partial y^2}+\frac{\partial^2\langle w\rangle}{\partial z^2}\right)-\frac{\partial\langle v'w'\rangle}{\partial y}-\frac{\partial\langle w'w'\rangle}{\partial z}-Ro\tau_1\langle v\rangle-(z-z_0)\frac{Gr}{Re_\tau^2}\langle\Theta\rangle \tag{6}$$

In Eqs. (5) and (6) there are four terms in vector form with different physical meaning, i.e., the pressure gradient (D_P), the turbulent stress gradient (D_S), the Coriolis force (D_C) and the centrifugal buoyancy force (D_B):

D_P: $(-\partial\langle p\rangle/\partial y, -\partial\langle p\rangle/\partial z)$,
D_S: $(-\partial\langle v'v'\rangle/\partial y-\partial\langle v'w'\rangle/\partial z, -\partial\langle v'w'\rangle/\partial y-\partial\langle w'w'\rangle/\partial z)$,
D_c: $(Ro_{\tau1}\langle w\rangle, -Ro_{\tau1}\langle v\rangle)$,
D_B: $(-(y-y_0)Gr/\mathrm{Re}_\tau^2\langle\Theta\rangle, -(z-z_0)Gr/Re_\tau^2\langle\Theta\rangle)$.

In the above expressions <·> denotes ensemble average.

Fig. 5 shows the distributions of D_P, $D_P + D_S$, $D_P + D_S + D_C$, $D_P + D_S + D_C + D_B$ in cross-section plane at Grashof number

Table 2
The averaged value of physical parameters at different computational conditions.

	Re			U_b	$100\,k/U_b^2$	Nu	$f\times10^3$
$Ro = 5.0$	Case 1	5999	$Gr = 10^6$	15.01	1.52	9.28	8.89
	Case 2	6068		15.17	1.51	9.19	8.69
	Case 3	5984		14.96	1.51	6.88	8.94
	Case 4	5966		14.91	1.53	10.17	8.99

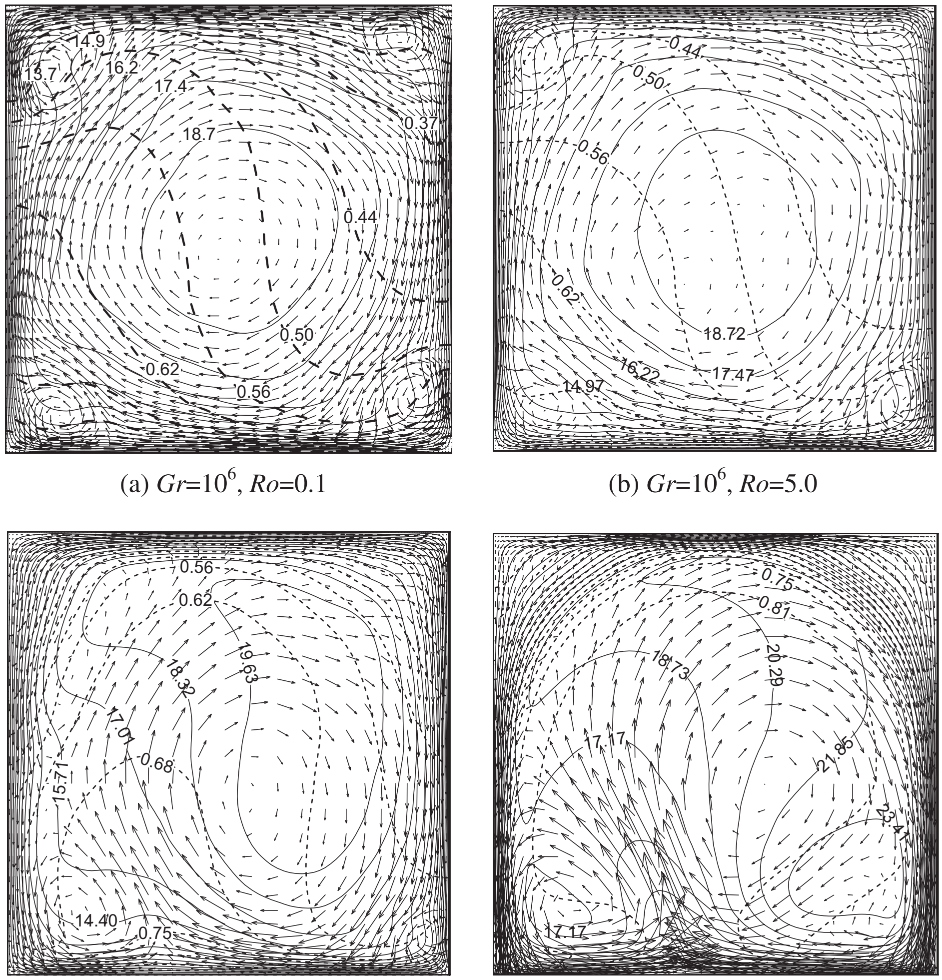

(a) $Gr=10^6$, $Ro=0.1$ (b) $Gr=10^6$, $Ro=5.0$

(c) $Gr=10^7$, $Ro=5.0$ (d) $Gr=10^8$, $Ro=5.0$

Fig. 4. Velocity and temperature fields under different situations for Case 1.

$Gr = 10^6$ for Case 1. It is observed that pressure gradient is the major driving force. Distributions of $D_P + D_S$ and $D_P + D_S + D_C$ are in good accordance with that of D_P, which shows that the Reynolds stress and Coriolis force have no appreciable effects on generation of secondary flow. Fig. 5(d) shows that centrifugal buoyancy force opposes the pressure driving, resulting in the reduction of secondary flow compared with the nonrotating flow [15]. Similar analyses can be made for the other three cases and Grashof numbers, and all the results come to the same conclusion that the forces balance in cross section determines the flow pattern. For the simplicity of presentation such analyses are omitted here.

4.2. Turbulence intensities

Fig. 6 shows the root mean square (r.m.s) of velocity and temperature fluctuations along the wall bisectors perpendicular to the isothermal walls. With the increase of Grashof number, the intensities of velocity fluctuations are strengthened near the bottom wall while suppressed near the top wall (Fig. 6(a)), which is similar to that in a rotating channel flow [2]. In Fig. 6(b), the intensities of temperature fluctuation decrease with the increase of Grashof number and profiles of r.m.s become asymmetrical to $y = 0.5$ for Case 1. When Grashof number increases to $Gr = 10^7$, the intensities of temperature fluctuation near the top wall are stronger than that of the bottom side, while at $Gr = 10^8$ fluctuations near the bottom wall are stronger than that of the top side.

4.3. Momentum budget

Analysis of the mechanisms that affect the averaged streamwise velocity was made by examining the terms of the resolved dimensionless Reynolds averaged U-momentum equation. For a fully developed flow, the dimensionless Reynolds averaged U-momentum equation can be written in the form of Eq. (7)

$$\underbrace{-\langle v\rangle\frac{\partial\langle u\rangle}{\partial y}-\langle w\rangle\frac{\partial\langle u\rangle}{\partial z}}_{convection}\underbrace{-\frac{\partial\langle u'v'\rangle}{\partial y}-\frac{\partial\langle u'w'\rangle}{\partial z}}_{turbulent\ \ transport}+\underbrace{\frac{1}{Re_\tau}\left(\frac{\partial^2\langle u\rangle}{\partial y^2}+\frac{\partial^2\langle u\rangle}{\partial z^2}\right)}_{diffusion}=\underbrace{-4}_{mean\ \ pressure\ \ gradient} \tag{7}$$

The terms of Eq. (7) are responsible for, from left to right, convection, turbulent transport, viscous diffusion and pressure gradient. In the following figures, convective term, pressure gradient term, viscous term, turbulent transport term are denoted as CONV, PG, VD, TD, respectively, and the rest terms are denoted as RES. The terms in the U-equation along wall bisectors for $Ro = 5.0$ and $Gr = 10^6$ for four cases are plotted in Fig. 7. The spatial distributions of the different terms in Fig. 7 are qualitatively the same as mentioned by Huser and Biringen [8] for the nonrotating turbulent duct flow as well as Pallares and Davidson [10,11] for the orthogonally

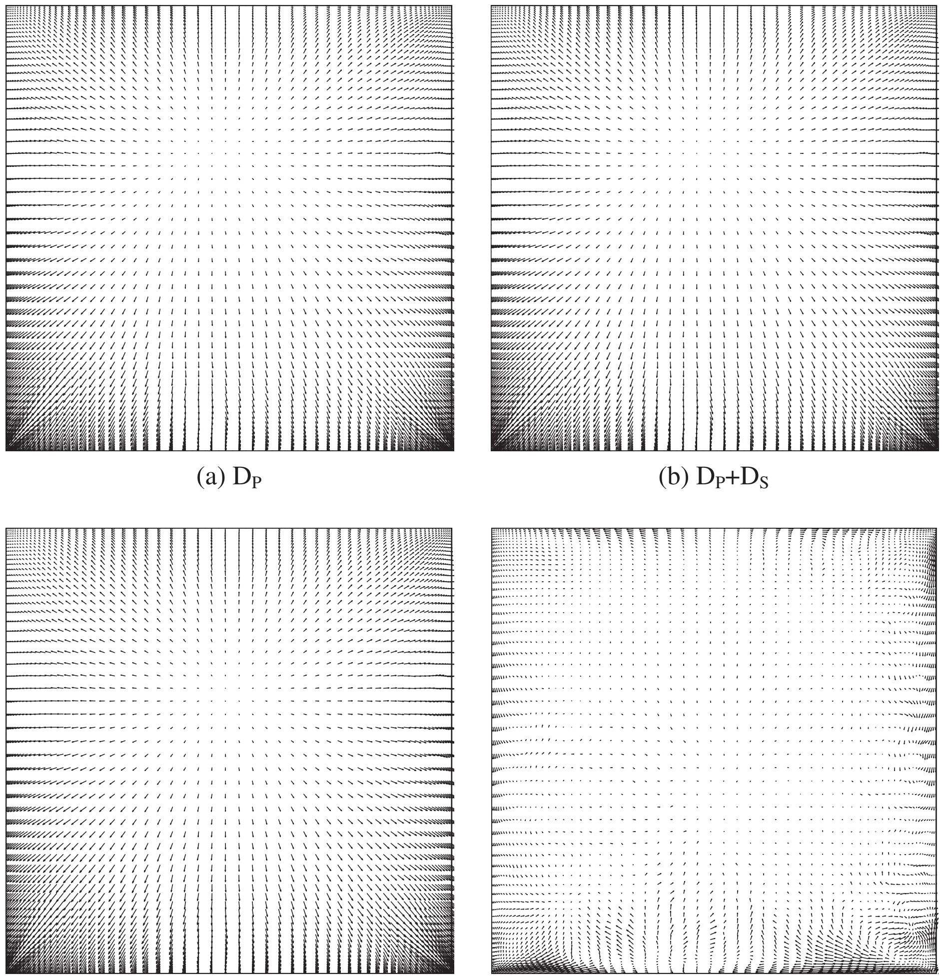

(a) D_P (b) D_P+D_S

(c) $D_P+D_S+D_C$ (d) $D_P+D_S+D_C+D_B$

Fig. 5. The distributions of D_P, D_P+D_S, $D_P+D_S+D_C$, $D_P+D_S+D_C+D_B$ at $Gr = 10^6$ for Case 1.

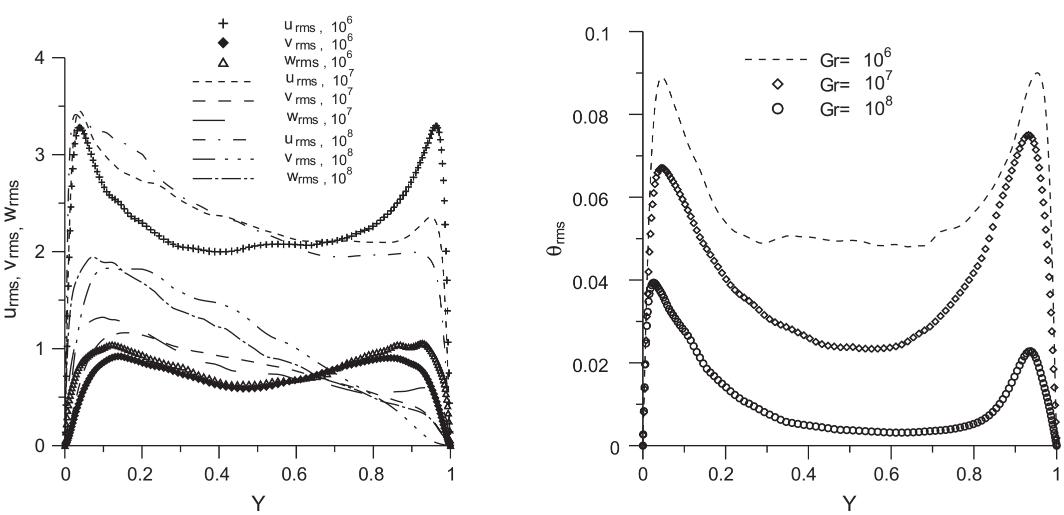

(a) Root mean square of fluctuation velocity of Case 1 (b) Root mean square of fluctuation temperature of Case 1

Fig. 6. Intensities of root mean square of fluctuation quantities.

rotating duct flow. Graphs corresponding to four cases (Figs. 7(a)–(d)) have no great different characteristics of distribution for each term in Eq. (7), thus thermal boundary conditions have no obvious effects on the role of terms in U-momentum equation. Also, Fig. 7

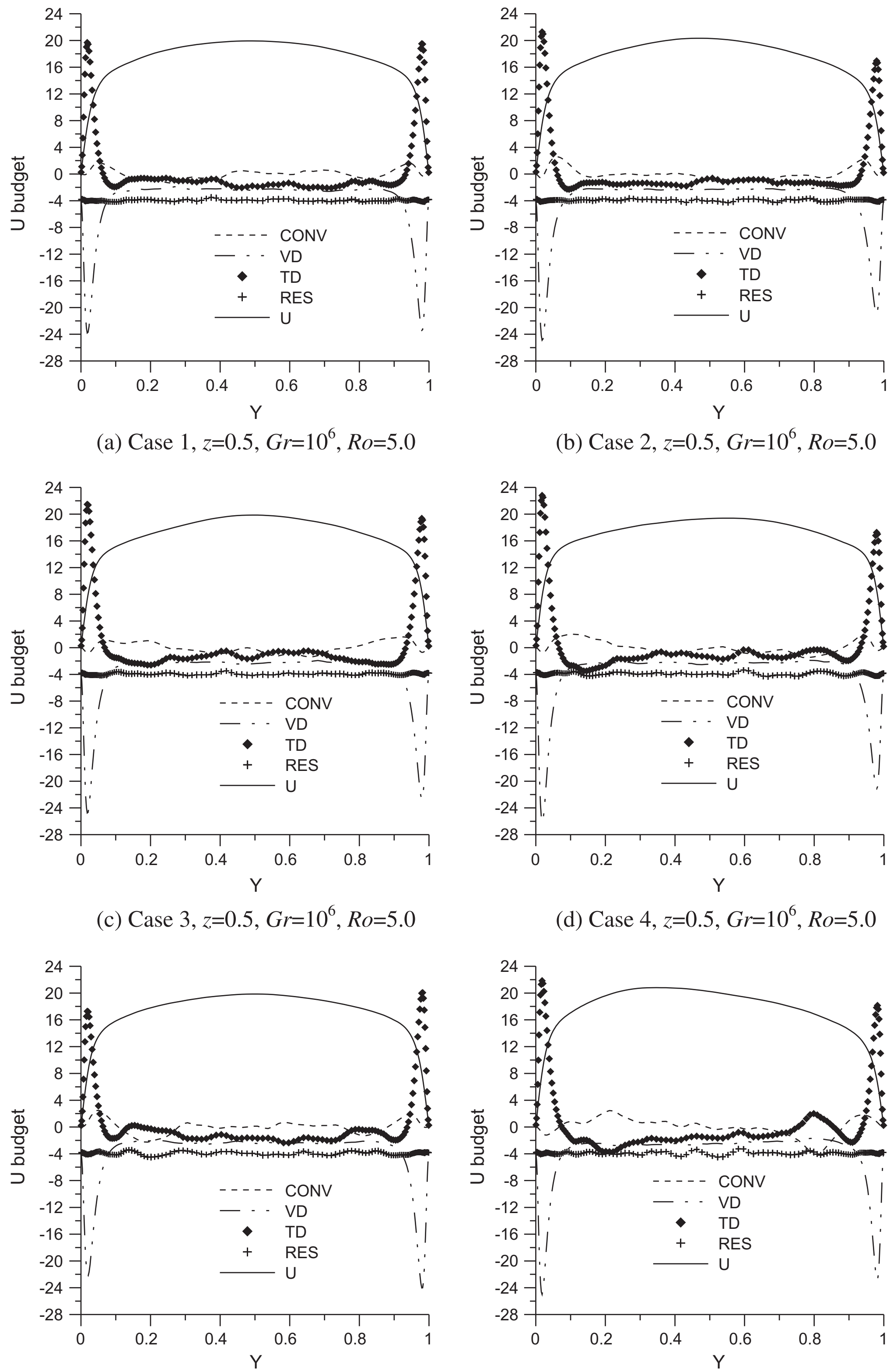

(a) Case 1, z=0.5, Gr=10^6, Ro=5.0
(b) Case 2, z=0.5, Gr=10^6, Ro=5.0
(c) Case 3, z=0.5, Gr=10^6, Ro=5.0
(d) Case 4, z=0.5, Gr=10^6, Ro=5.0
(e) Case 1, z=0.5, Gr=10^6, Ro=0.1
(f) Case 4, z=0.5, Gr=10^7, Ro=5.0

Fig. 7. Budgets of U-momentum along the vertical wall bisectors at Ro = 5.0 and Gr = 10^6.

shows that the convection term in four cases makes no significant contribution to the U-momentum budgets except for the near wall regions along wall bisectors. The main mechanisms for momentum transfer are viscous diffusion, turbulent transport and averaged pressure gradient. Close to the walls, viscous diffusion term mainly contributes to the loss of the momentum while turbulent transport term favors to the gain of momentum from central part of the duct. Fig. 7(e) shows the budget of U-momentum along vertical wall bisector for Case 1 at Ro = 0.1 and Gr = 10^6, which has no evident difference compared with that of Fig. 7(a)–(d). Fig. 7(f) shows distributions of terms in Eq. (7) at Grashof number $Gr = 10^7$, and it shows that convection has increased influence on balance of momentum compared with that of Fig. 7(d), especially near wall. Turbulent transfer has a larger contribution to the momentum budget in the bottom wall side than that in the top wall side, because the rotation destabilizes the flow and leads to the increase of turbulence in the bottom wall side, while in the top wall side, the turbulence is suppressed, especially for higher Grashof number cases.

4.4. Turbulence structure

Figs. 8–10 illustrate the low- and high-speed streak structures of fluctuating streamwise velocity and temperature in the x–z plane at $y^+ = 2.36$ for Case 1 at different rotation rates and Grashof numbers. Streak structures are associated with the formation of bursting event, which is the mechanism of the generation of Reynolds stress and turbulent kinetic energy [16]. In Fig. 8(a), the width between low- and high-speed streaks distributes nonuniformly. It indicates that the probability of bursting event is unequal. In the down region, the width of low- and high-speed streaks is smaller than that of the upper region, which means that bursting events take place more frequently in the down region. In Fig. 9(a), the width is reduced, which indicates that the bursting events take place more frequently than in Fig. 8(a). Therefore, the exchange of momentum and energy is strengthened. In Fig. 10(a) the Grashof number increases to $Gr = 10^7$, the width further decreases and the streak structures become more vigorously. This is resulted from more frequent ejection and sweep events stimulated by the increased buoyancy. The temperature fluctuations are consistent with the streamwise fluctuation velocity in the three pictures mentioned above. The locations of the high fluctuating temperature region are different from each other in the three pictures. In Fig. 8(b) the high temperature region is mainly in the

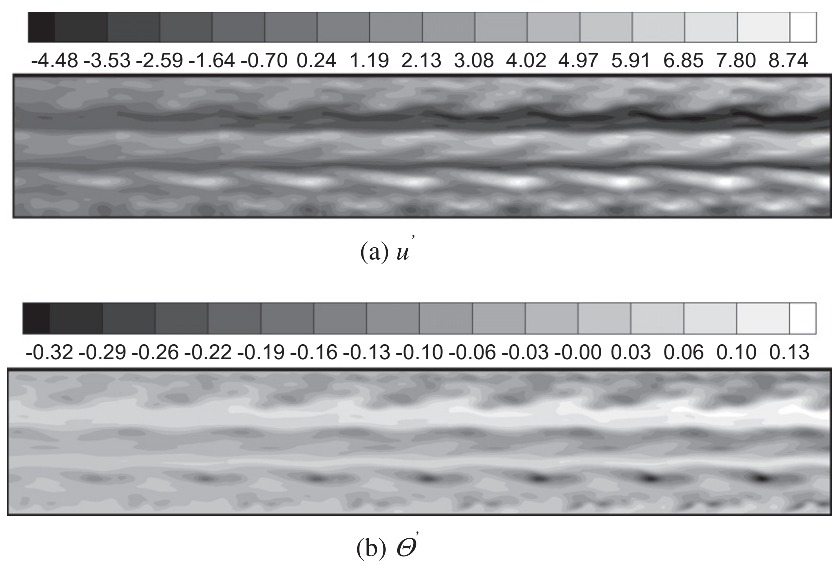

Fig. 8. Distributions of streamwise fluctuation velocity u' and fluctuation temperature Θ' on the x–z plane at $y^+ = 2.36$ for Case 1 at $Ro = 5.0$ and $Gr = 10^6$.

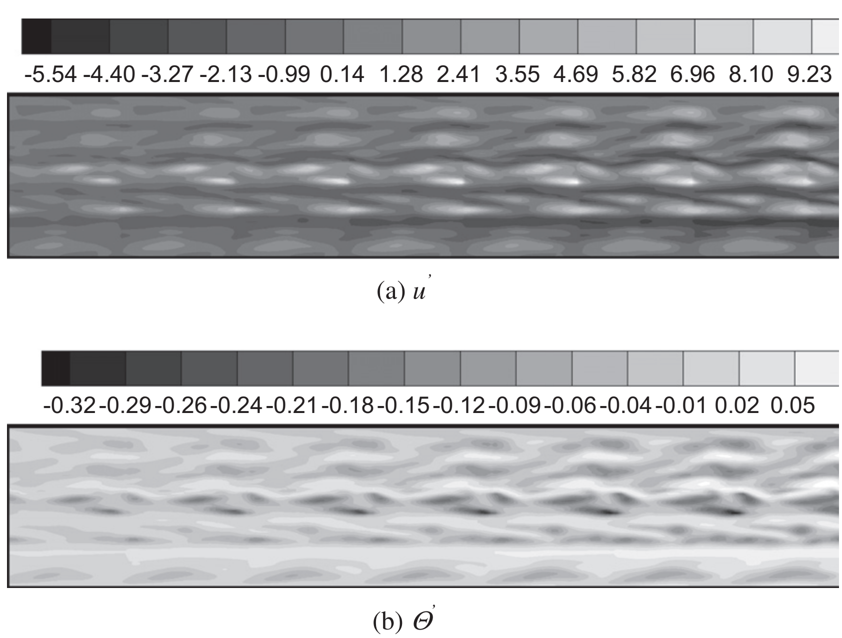

Fig. 9. Distributions of streamwise fluctuation velocity u' and fluctuation temperature Θ' on the x–z plane at $y^+ = 2.36$ for Case 1 at $Ro = 0.1$ and $Gr = 10^6$.

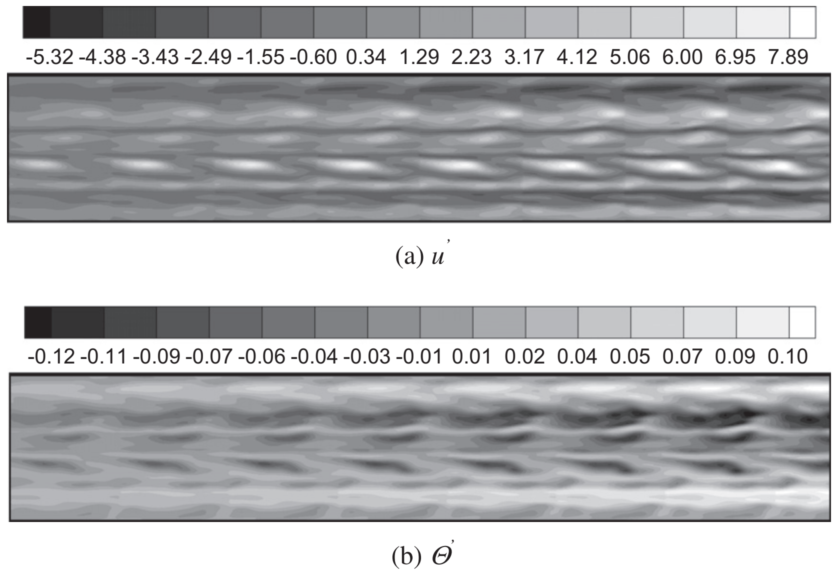

Fig. 10. Distributions of streamwise fluctuation velocity u' and fluctuation temperature Θ' on the x–z plane at $y^+ = 2.36$ for Case 1 at $Ro = 5.0$ and $Gr = 10^7$.

upper region; in Fig. 9(b) the high fluctuating temperature region locates in the down region; while in Fig. 10(b) temperature seems distributes symmetrically about the centerline.

Finally it may be noted that in the present study the stress Reynolds number $Re_\tau = 400$ was picked, which corresponds a duct Reynolds number about 6000 defined by bulk averaged velocity U_b. In DNS this is quite a high Reynolds number being simulated. For example to the authors' knowledge, in the previous studies [9,7] the cases of $Re_\tau = 300$ (corresponds a Reynolds number defined by bulk averaged streamwise velocity of about 4400) was conducted. Although the results of the present study may include some effects of low Reynolds number flow, the major physical features influenced by the thermal boundaries and the buoyancy force can still be revealed.

5. Conclusions

In this paper direct numerical simulations of turbulent flow and heat transfer at low Reynolds number in an axially rotating duct flow have been conducted for different thermal boundary conditions, rotation rates and Grashof numbers by using a self-developed second-order accuracy code. Three main conclusions are made from this study.

(1) The four thermal boundary conditions adopted in this paper have rather strong effects on the topology of secondary flow, distributions of axial velocity and temperature fields, and other turbulent statistic quantities. On the whole, the velocity fields for Case 1 and Case 2 have common features but the temperature distributions are obviously different, meanwhile, Case 3 and Case 4 have the same similarities and differences. The intensities of secondary flow for Case 1 and Case 2 are stronger than those for Case 3 and Case 4. And the streamwise velocity and temperature for Case 1 and Case 2 vary more drastically than those for Case 3 and Case 4, especially near the wall. But, there are no evident differences in bulk averaged streamwise velocity, turbulent kinetic energy, and friction factors as well as U-momentum budget when different thermal boundary conditions are adopted.

(2) In the axially rotating duct flow studied Coriolis force induced by rotation has marginal effects on velocity and temperature fields, turbulent statistics quantities, momentum budget because the Coriolis force exerts on the y–z plane and has a small magnitude.

(3) Buoyancy force, the product of centrifugal force and density gradient, takes a key role on the development of velocity and temperature fields. Buoyancy is the major mechanism of developing secondary flow under the conditions presented in this paper. With the increase of the Grashof number, the buoyancy effects increase and the intensities of cross-section flow are enhanced more and more obviously. With the increase of buoyancy, the distributions of streamwise velocity and temperature fields are changed, including the change of pattern, variation of level and drifting the maximum value of axial velocity and the minimum value of temperature to the side walls. Further, with the increase of Grashof number, intensities of fluctuation velocities and temperature increase on the bottom wall side and decrease on the top wall side for Case 1.

Acknowledgments

The authors are gratefully to the financial support by the National Nature Science Foundation of China (No. 50636050), and also gratefully appreciate for the support of Shanghai Supercomputer Center (China) in using its high performance computing facilities and technical support.

References

[1] D.K. Tafti, S.P. Vanka, A numerical study of the effects of spanwise rotation on turbulent channel flow, Phys. Fluids A 3 (1991) 642–656.
[2] R. Kristoffersen, H. Andersson, Direct simulations of low-Reynolds number turbulent flow in a rotating channel, J. Fluid Mech. 256 (1993) 163–197.
[3] O. Iida, N. Kasigi, Direct numerical simulation of unstably stratified turbulent channel flow, ASME J. Heat Transfer 119 (1997) 53–61.
[4] H.B. Wu, N. Kasagi, Effects of combined spanwise and streamwise rotations on turbulent channel flow, in: Proceedings of 5th JSME–KSME Fluids Engineering Conference, Nagoya, 2002.
[5] J.H. Wagner, B.V. Johnson, R.A. Graziani, E.C. Yeh, Heat transfer in rotating serpentine passages with trips normal to the flow, ASME J. Turbomach. 14 (1992) 847–857.
[6] B.E. Lounder, W.M. Ying, Secondary flows in ducts of square cross-section, J. Fluid Mech. 54 (1972) 289–295.
[7] S. Gavrilakis, Numerical simulation of low-Reynolds number turbulent flow through a straight square duct, J. Fluid Mech. 244 (1992) 101–129.

[8] A. Huser, S. Biringen, Direct numerical simulation of turbulent flow in a square duct, J. Fluid Mech. 257 (1993) 65–95.
[9] M. Piller, E. Nobile, Direct numerical simulation of turbulent heat transfer in a square duct, Int. J. Numer. Methods Heat Fluid Flow 12 (2002) 658–686.
[10] L. Pallares, L. Davidson, Large-eddy simulations of turbulent flow in a rotating square duct, Phys. Fluids 12 (2000) 2878–2893.
[11] L. Pallares, L. Davidson, Large-eddy simulations of turbulent heat transfer in stationary and rotating square duct, Phys. Fluids 14 (2002) 2804–2816.
[12] Z.H.H. Qin, R.H. Pletcher, Large eddy simulation of turbulent heat transfer in a rotating square duct, Int. J. Heat Fluid Flow 27 (2006) 371–390.
[13] N. Kasagi, M. Nishimura, Direct numerical simulation of combined forced and natural turbulent convection in a vertical plane channel, Int. J. Heat Fluid Flow 18 (1996) 88–99.
[14] T. Kajishima, Y. Miyake, A discussion on eddy viscosity models on the basis of the large eddy simulation of turbulent flow in a square duct, Comput. Fluids 21 (1992) 151–161.
[15] L.D. Ma, Experimental study of the fundamental mechanism in enhanced heat transfer and the advanced numerical simulation of turbulent heat transfer in rectangular duct. School of Energy & Power Engineering, Xi'an JiaoTong University, Xi'an, 2007.
[16] S.K. Robinson, Coherent motions in turbulent boundary layer, Ann. Rev. Fluid Mech. 23 (1991) 601.